research papers

Energy separation of neutrons scattered at small angles from silicon using time-of-flight techniques

J. Y. Cheung,[a] R. J. Stewart[a]* and R. P. May[b]

[a]J. J. Thomson Physical Laboratory, University of Reading, Whiteknights, Reading RG6 6AF, England, and [b]Large Scale Structures Group, Institut Laue–Langevin, 6 rue Jules Horowitz, Grenoble CEDEX 9, F-38042, France. Correspondence e-mail: r.j.stewart@reading.ac.uk

The time-of-flight technique is used on a small-angle neutron scattering instrument to separate the energies of the scattered neutrons, in order to determine the origin of the temperature-dependent scattering observed from silicon at $Q > {\sim}0.1$ Å^{-1}. A quantitative analysis of the results in comparison with the phonon dispersion curves, determined by Dolling using a triple-axis neutron spectrometer, shows that the temperature-dependent scattering can be understood in terms of Umklapp processes whereby neutrons gain energy from phonons.

1. Introduction

Beddoe *et al.* (1983) reported anisotropic temperature-dependent small-angle neutron scattering (SANS) from Czochralski-grown silicon when the incident neutron beam was along a [111] direction. These measurements were made using the D11 (Ibel, 1976) and D17 SANS instruments at the Institut Laue–Langevin (ILL), Grenoble, France. Subsequently, Gupta *et al.* (1992) reported similar temperature-dependent scattering from silicon when the incident neutron beam was along a [100] direction. This temperature-dependent scattering was observed when short sample-to-detector distances (around 1 m) were used with neutrons in the range 6–10 Å. The anisotropic scattering at the edges of the detector, seen in the contour plot of the scattered neutron intensity shown in Fig. 1, is an example of this temperature-dependent scattering. The cross-shaped scattering recorded at the centre of the detector arises from elastic scattering from SiO_2 precipitates in the silicon crystal. It was suggested by Beddoe *et al.* (1983) that one possible explanation for this temperature-dependent scattering might be inelastic processes and they carried out an experiment to determine whether the scattering was due to elastic or inelastic processes. This was performed using the D17 SANS instrument, with a chopper installed, which pulsed the incident neutron beam, thus enabling the time of flight (TOF) of the scattered neutrons to be recorded. The detector electronics available at the time were limited by memory constraints to a total of 16384 channels. Thus, in order to carry out the time-of-flight experiment, the spatial resolution of the detector had to be reduced from 16384 5×5 mm detector elements to 1024 20×20 mm detector elements. This reduction was achieved by grouping the output of 16 of the 5×5 mm detector elements together and recording the output in one memory channel. This process enabled 16 two-dimensional detector scattering patterns to be sequentially recorded, each lasting 240 µs, to produce a set of TOF data for each neutron pulse from the chopper. No measurable inelastic scattering was seen. Beddoe *et al.* (1983) thus concluded that the temperature-dependent scattering possibly arose from a modification of the dispersion curves in the centre of the Brillouin zone owing to the presence of SiO_2 precipitates. The studies of Gupta *et al.* (1992) showed that the temperature-dependent scattering was not due to changes in the silicon phonon curves caused by oxygen precipitates in the matrix, since the magnitude and form of the temperature-dependent scattering was the same irrespective of the size, shape or distribution of the oxygen precipitates. Indeed, they observed the temperature-dependent scattering in a nominally oxygen-free float-zone-grown silicon crystal.

With the increase in neutron flux available on the D22 SANS instrument at the ILL (May, 2000) compared with D17, and the larger detector electronics memory now available, a further experiment was carried out using time-of-flight analysis and the full spatial resolution of the area detector on D22. The aim was to reinvestigate, with higher incident neutron flux and enhanced time and spatial resolution, whether the anisotropic temperature-dependent scattering had its origin in inelastic processes.

2. Theoretical background

Inelastic scattering studies can show how neutrons interact with the lattice vibrations of a crystalline sample. Neutrons of different energies enter the sample and they can either gain energy (+) or lose energy (−) by creating or absorbing lattice vibrations, that is phonons of wavevector **q**. Energy conservation must hold; therefore

$$\frac{\hbar^2 k_{\mathrm{f}}^2}{2m_{\mathrm{n}}} - \frac{\hbar^2 k_{\mathrm{i}}^2}{2m_{\mathrm{n}}} = \pm\hbar\omega, \qquad (1)$$
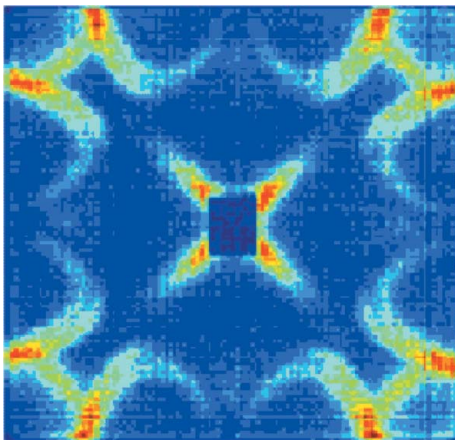
Figure 1
Contour map of the anisotropic scattering from a silicon single crystal oriented with the [100] direction along the incident neutron beamline. Neutron wavelength = 8 Å and sample–detector distance = 1.5 m
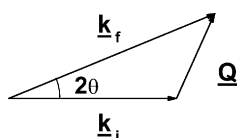
Figure 2
Vector diagram of the scattering process

where $\hbar$ is Planck's constant, h, divided by 2π, k_i is the magnitude of the wavevector of incident neutrons ($\mathbf{k}_i$), k_f is the magnitude of the wavevector of the scattered neutrons ($\mathbf{k}_f$), ω is the phonon angular frequency and m_n is the neutron mass.

From momentum conservation, the difference $\mathbf{k}_f - \mathbf{k}_i$ must be equal to $\mathbf{Q}$, where $\mathbf{Q}$ is the scattering vector (Fig. 2):

$$k_f - k_i = Q. \qquad (2)$$

Using the cosine rule, we obtain an expression for Q^2,

$$Q^2 = k_f^2 + k_i^2 - 2k_i k_f \cos 2\theta, \qquad (3)$$

where Q is the magnitude of the scattering vector $\mathbf{Q}$ and 2θ is the scattering angle.

Substituting k_f^2 with the value determined from equation (1), we arrive at the following expression for Q^2:

$$Q^2 = 2\left[k_i^2 \pm \frac{m_n \omega}{\hbar} - k_i \cos 2\theta \left(k_i^2 \pm \frac{2m_n \omega}{\hbar} \right)^{1/2} \right]. \qquad (4)$$

Values of Q were calculated using equation (4) for neutron energy gain (+) and neutron energy loss (−) through phonon interaction at two scattering angles: $2\theta = 0°$ and $2\theta = 24.3°$, where the latter is the maximum scattering angle of 2θ on D22 with the sample-to-detector distance set to 1.5 m. The loci of allowable ω and Q values are plotted in Fig. 3. The incident neutrons used had an energy of 1.3 meV (wavelength of 8 Å). Thus phonons with energy greater than this cannot be created. The maximum phonon frequency that could theoretically be created is thus $\omega = 1.9$ Trad s^{-1}. Thus in Fig. 3, the loci of allowable ω and Q values stop at $\omega = -1.9$ Trad s^{-1}. The Brillouin zone boundary in the [100] direction in silicon is at $Q = 1.157$ Å^{-1}; thus the allowable ω and Q values are trun-
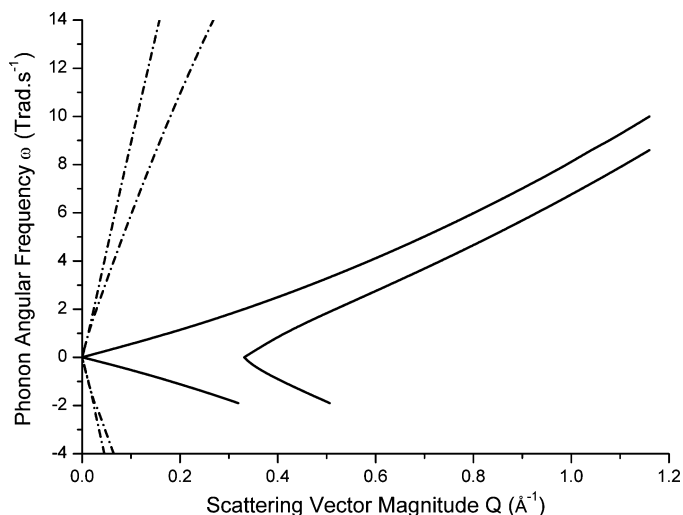
Figure 3
Loci of allowable ω and Q values (solid lines) on D22 with a sample-to-detector distance of 1.5 m for neutron energy loss (phonon creation) or neutron energy gain (phonon annihilation). The left and right solid lines correspond to scattering angles (2θ) of 0 and 24.3°, respectively. The dot–dash lines are fits to the silicon dispersion curves for the [100] direction from Dolling (1963).

cated at $Q = 1.157$ Å^{-1}. The phonon dispersion curves for silicon were obtained by Dolling (1963) using the 'constant Q' technique on the triple-axis spectrometer at the NRU reactor, Chalk River. Three crystallographic directions of a single crystal of pure silicon were studied. Those for the [100] direction have been fitted and are shown by the dotted lines in Fig. 3. In order to create or annihilate a phonon, part of the dispersion curve must intersect the experimentally defined loci of allowable ω and Q values in order to conserve both energy and momentum in the neutron–phonon interaction. This intersection does not occur for phonon creation (see Fig. 3) and thus for 8 Å neutrons impinging on a silicon single crystal only phonon annihilation processes are allowed. From Fig. 3 it is also clear that there is no intersection corresponding to phonon annihilation in the first Brillouin zone (*i.e.* corresponding to a normal process).

Fig. 4 shows the loci of allowable ω and Q values, based on the D22 instrument parameters used, superimposed on Dolling's dispersion curves for the [100] direction (the direction in which the neutron beam impinged on the silicon in the TOF experiment). A reduced zone scheme is used so that all possible phonon annihilation processes are included (*i.e.* both normal and Umklapp).

3. Experimental details

A sample that had been heat-treated for 500 h at 873 K, and for 1000 h at 773 K, was studied on D22 with the time-of-flight chopper in place (see Fig. 5).

A time-of-flight chopper was placed just before the sample area of the D22 instrument at the ILL. A continuous colli-mated neutron beam, originating from a velocity selector set to transmit 8 Å neutrons, impinges onto the chopper. A collimation distance of 2.8 m was chosen to match the angular
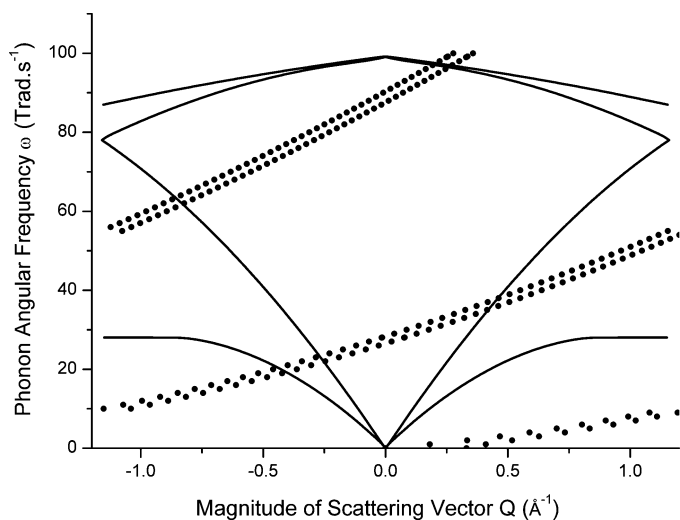
Figure 4
Loci of allowable ω and Q values (dotted lines) on D22 with a sample-to-detector distance of 1.5 m for neutron energy gain (phonon annihilation). A reduced zone scheme is used so that all possible phonon annihilation processes are included (normal and Umklapp). The upper and lower dotted lines correspond to scattering angles (2θ) of 0 and 24.3°, respectively. The solid lines are fits to the silicon dispersion curves for the [100] direction under the reduced zone scheme from Dolling (1963).
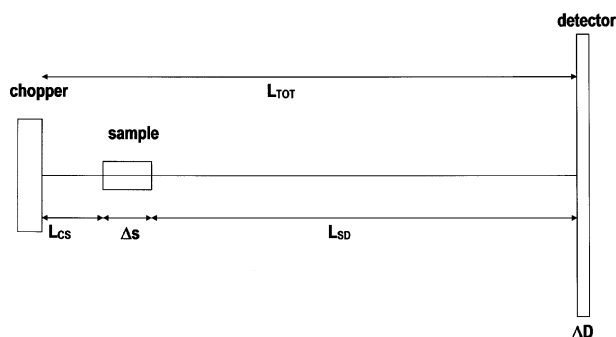

Figure 5
Schematic diagram of the D22 instrument with a time-of-flight chopper. L are distances and in the subscripts C refers to the chopper, S to the sample, D to the detector and TOT to the total flight path. ΔD refers to the detector thickness and ΔS to the sample thickness.

resolution of the detector for the 1.5 m sample-to-detector distance employed in these experiments. The time-of-flight chopper consists of a disc made of highly neutron-absorbing material into which two openings are machined, thus producing two neutron pulses per revolution of the disc. The pulse separation of 25 ms is determined by the chosen rotation speed of the disc (1200 r.p.m.). The pulsed monochromatic neutron beam then impinges on the heat-treated silicon crystal being studied. A cadmium plate, with an aperture cut in it of 10 mm diameter, determined the size of the neutron beam; this was placed just in front of the sample. A large cadmium plate, with an aperture of 14 mm diameter cut in it, was positioned just before the chopper to reduce the thermal and cold neutron background signal. The neutrons scattered by the sample are detected using a two-dimensional He^3 position-sensitive detector. The detector consists of a 128 × 128 array of detector elements, each of size 7.5 × 7.5 mm; this was
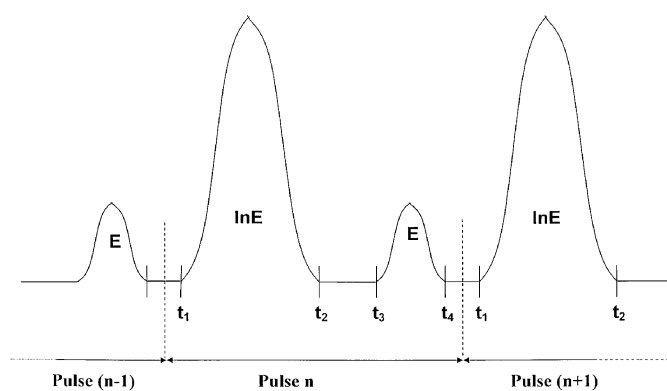

Figure 6
Schematic diagram showing the form of the elastic and inelastic peaks for the nth neutron pulse. InE are inelastic peaks and E are elastic peaks.

positioned 1.5 m from the sample. The time of arrival of the detected neutrons was sorted into 50 time channels, each of 125 µs duration. The first time channel was triggered after a time delay. This process would repeat itself for a set amount of time. Three sets of runs were carried out, each run lasting 1 h. For each time channel, a two-dimensional record of the distribution of neutrons detected was recorded; each of these was assigned a run number and the TOF spectra obtained clearly showed that the elastic scattering from oxygen-containing precipitates could be separated in time from the temperature-dependent scattering (see §4). Empty can, cadmium and calibration runs were also carried out for 1 h each.

3.1. Experimental background

Assuming that some of the neutrons were inelastically scattered and some were elastically scattered, the variation in scattered neutron intensity with time of flight will follow a general trend, as indicated by Fig. 6. The times of flight of neutrons, in microseconds, arriving at the times t_1, t_2, t_3 and t_4, indicated in Fig. 6, can be calculated using:

$$\text{Time of flight} = (m_n/h)\lambda L = 252.78\lambda\,(\text{Å}) \times L\,(\text{m}), \quad (5)$$

where λ is the neutron wavelength in ångströms and L is the distance travelled by the neutron in metres.

Fig. 7 is a schematic diagram of the experimental setup, showing the neutron paths and how the fastest and slowest elastically and inelastically scattered neutrons are related to the times t_1, t_2, t_3 and t_4 (measured in microseconds);

$$t_1 = 252.78\,[\lambda_{min}L_{CS} + (\lambda_{min} - \Delta\lambda_{max})(\Delta s + L_{SD})], \quad (6)$$

$$\begin{aligned} t_2 = 252.78\,[\lambda_{max}(L_{CS} + \Delta s) + (\lambda_{max} - \Delta\lambda_{min}) \\ \times (L_{SD} + \Delta D)] + \Delta t_{on}, \end{aligned} \quad (7)$$

$$t_3 = 252.78\lambda_{min}(L_{CS} + \Delta s + L_{SD}), \quad (8)$$

$$t_4 = 252.78\lambda_{max}(L_{CS} + \Delta s + L_{SD} + \Delta D) + \Delta t_{on}. \quad (9)$$

λ_{min} corresponds to the wavelength (in ångströms) of the fastest neutrons coming from the chopper and λ_{max} is the

wavelength (in ångströms) of the slowest neutrons. L_{CS} is the distance (in metres) between the chopper and the sample, L_{SD} is the distance (in metres) between the sample and the detector and Δs is the thickness of the sample (in metres). Finally, Δt_{on} is the total time (in microseconds) during which the chopper window allows neutrons to be transmitted. The chopper, to a first approximation, gives the same distribution of neutron wavelengths between $\pm 10\%$ of the mean wavelength as set by the helical velocity selector. In these experiments, the helical velocity selector was set to allow 8 Å neutrons through to the chopper. Therefore, $\lambda_{min} = 7.2$ Å to $\lambda_{max} = 8.8$ Å, to a good approximation, is the range of wavelengths coming through the chopper windows. (These values were confirmed in the experiment from the time-of-flight analysis.)

The energy of a neutron E (meV) corresponding to a wavelength λ (Å) can be obtained using the following expression:

$$E(\text{meV}) = 81.81/\lambda^2\,(\text{Å}^2). \qquad (10)$$

This expression can then be used to find the minimum and maximum energies that can be imparted to the neutrons by the phonons:

$$\Delta E_{min}(\text{meV}) = \frac{81.81}{(\lambda_{max} - \lambda_{min})^2} - \frac{81.81}{\lambda_{max}^2}, \qquad (11)$$

$$\Delta E_{max}(\text{meV}) = \frac{81.81}{(\lambda_{min} - \lambda_{max})^2} - \frac{81.81}{\lambda_{min}^2}. \qquad (12)$$

To convert from the phonon energy (meV) to the corresponding phonon angular frequency ω (Trad s^{-1}) the following relation is used:

$$\Delta\omega\left(\text{Trad s}^{-1}\right) \simeq 3\Delta E(\text{meV})/2. \qquad (13)$$
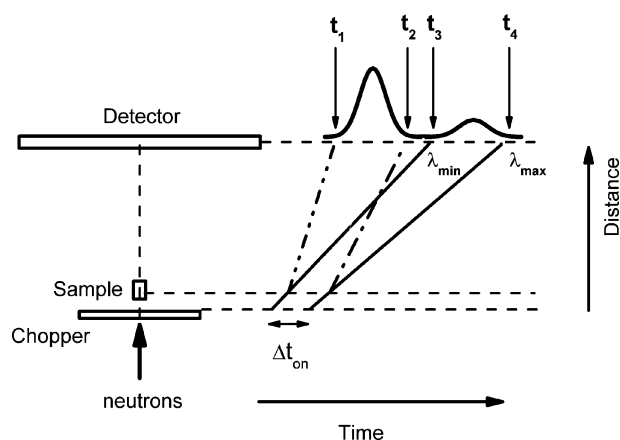

Figure 7
Schematic diagram of neutron flight paths. The dash–dot–dot line is for the shortest wavelength incident neutron (λ_{min}) at the start of the chopper pulse gaining the maximum energy from the phonons in the sample ($\lambda_{min} - \Delta\lambda_{max}$). The dash–dot line is for the longest wavelength (λ_{max}) at the end of the chopper pulse gaining the minimum energy from phonons in the sample ($\lambda_{max} - \Delta\lambda_{min}$).

Table 1
Experimental and calculated times of flight.

	Calculated time + offset of 240 µs	TOF channel No.	Experimental time channel × 125 µs	$\Delta\lambda_{max}$ (Å)	$\Delta\lambda_{min}$ (Å)
$t_{1,min}$	1622	13	1625	4.9	–
$t_{2,max}$	3627	29	3625	–	5.0
$t_{3,min}$	3534	29	3625	–	–
$t_{4,max}$	5750	46	5750	–	–

4. Results

The sequence of neutron small-angle scattering patterns obtained for each time-of-flight channel is displayed in Fig. 8. The figures show that it is possible to separate most of the inelastic scattering (TOF channels 16–23) from the elastic scattering (TOF channels 36–43). A plot of the total amount of scattering recorded over the whole detector is plotted against time-of-flight channel in Fig. 9. This plot is used to pinpoint the shortest times for t_1 and t_3 and the longest times for t_2 and t_4 described in equations (6)–(9), in terms of time channels. The times calculated using these equations would refer to the maximum values for t_1, t_2, t_3 and t_4 for neutrons travelling to the very edge of the detector and minimum values for neutrons that travel the least distance to the centre of the detector. The most important times are those that can be pinpointed on the TOF spectra, $t_{1,min}$, $t_{2,max}$, $t_{3,min}$ and $t_{4,max}$.

The experimental values of times of flight are calculated by multiplying the time-channel number (1–49), where the fastest/slowest elastic/inelastic neutrons arrive, by the channel width of 125 µs. For example, the slowest elastically scattered neutrons are seen to arrive in channel 46, therefore $t_4 = 125 \times 46 = 5750$ µs. The calculated value, using equation (9), gives a value of 5510 µs. The difference of 240 µs between these two values is due to the relative position of the chopper start pulse, which triggers the time-of-flight electronics. Therefore, this value must be added to all the calculated times. The experimental values of $t_{1,min}$, $t_{2,max}$, $t_{3,min}$ and $t_{4,max}$ are taken from Fig. 9 and compared with the calculated values in Table 1. The values of $\Delta\lambda_{min}$ and $\Delta\lambda_{max}$ are determined from the experimental values for $t_{1,min}$ and $t_{2,max}$ using equations (6) and (7). Using these values of $\Delta\lambda_{min}$ and $\Delta\lambda_{max}$, the energy transfers are calculated using equations (11), (12) and (13). The maximum and minimum energy transfers possible are thus given by

$$4.5 < E < 13.2\,\text{meV},$$

or in terms of phonon angular frequencies

$$6.8 < \omega < 19.9\,\text{Trad s}^{-1}. \qquad (14)$$

A coincidence of the loci of allowable ω and Q values from the experiment with Dolling's dispersion curve for a [100] direction in silicon occurs at $\omega = 19$ Trad s^{-1} and involves an Umklapp process (see Fig. 10).
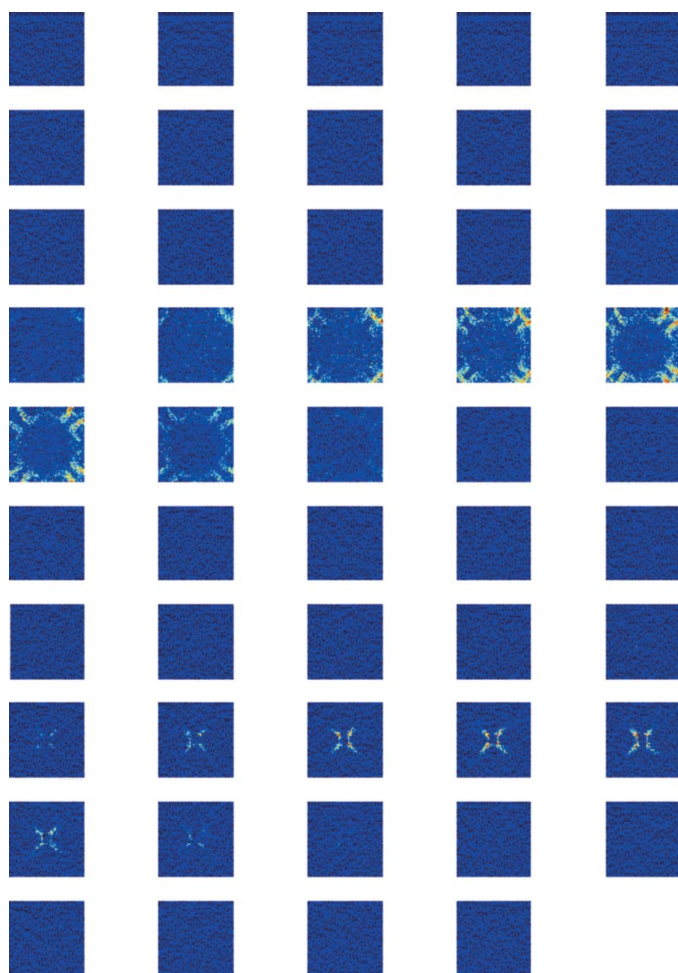
Figure 9
Measured time-of-flight spectra showing elastic (right-hand peak) and inelastic (left-hand peak) scattering. The vertical arrows at time channels 13, 29 and 46 mark the limits of elastically and inelastically scattered neutrons. Time channel 13 marks the fastest detected inelastically scattered neutron. Time channel 29 separates the slowest detected inelastically scattered neutron and the fastest detected elastically scattered neutron. Time channel 46 marks the slowest detected elastically scattered neutron.

Figure 8
Sequence of time-of-flight patterns from time channels 1–49 (silicon sample annealed for 500 h at 873 K and 1000 h at 773 K).

5. Discussion

These experiments have shown that the temperature-dependent scattering seen at the edges of the detector is the result of inelastic processes. A quantitative analysis of the energies and momentums involved suggests that these are Umklapp processes whereby the phonons impart energy to the impinging neutrons. One overlap between the loci of allowable ω and Q values and Dolling's dispersion curves for a [100] direction lies within the range of possible energy transfers given by equation (14).

The time of flight of the neutrons can also be represented as in Fig. 11, where the times of flight of the shortest and longest wavelength neutrons have been plotted. The times of flight of the slowest and fastest neutrons, having gained phonon energies of 13.2 and 4.5 meV, have also been plotted. Had the fastest and slowest neutrons gained phonon energies more or less than the range calculated here, then the time-of-flight spectra would have shown neutron counts in time channels outside those found (*i.e.* TOF channels < 13 or > 29). The TOF spectra show that there were no neutron counts above the background in these channels, and thus there were no
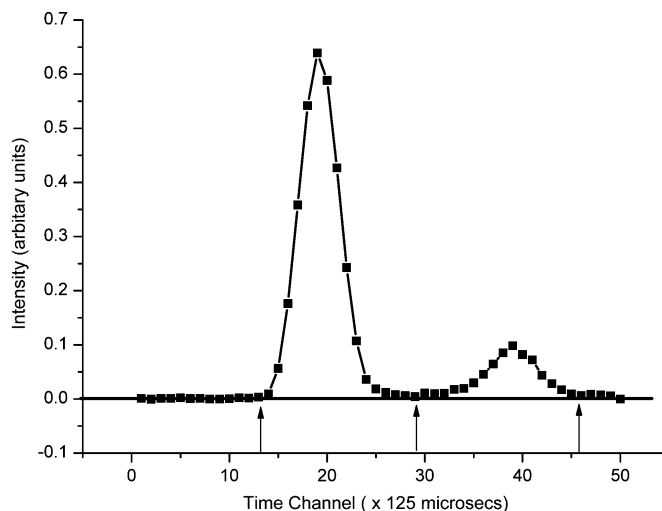
processes involving phonon energies greater than 13.2 or less than 4.5 meV.

Fig. 12 is a two-dimensional representation of a (100) section of the extended Brillouin zone of a face-centred cubic crystal. The magnitude of the scattered wavevector $k_{f,max}$ is the maximum possible value of k_f resulting from the annihilation of a phonon with the maximum possible energy in silicon of $\sim$66 meV ($\sim$100 Trad s^{-1} or $\sim$16 THz). The direction of $\mathbf{k}_{f,max}$ shown in Fig. 12 corresponds to the maximum scattering angle of the D22 set up with a sample-to-detector distance of 1.5 m. The directions of the vector $\mathbf{k}_f$ have also been drawn in Fig. 12 for three other scattering angles, corresponding to different
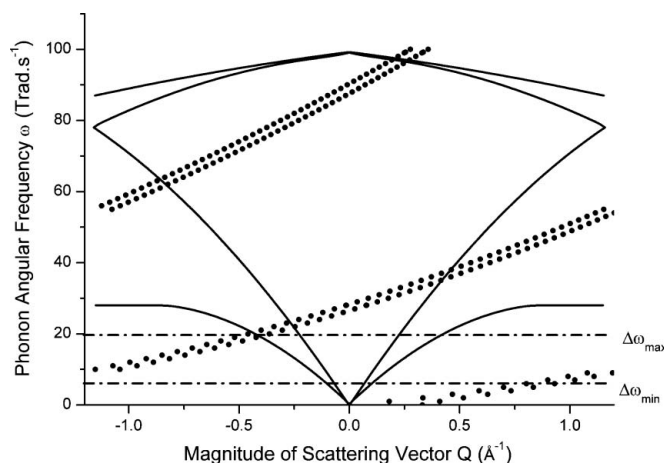

Figure 10
Dolling's dispersion curve for the [100] direction in silicon (solid lines) and the loci of allowable ω and Q values (dotted lines) on D22 with a sample-to-detector distance of 1.5 m. The upper and lower dotted lines correspond to scattering angles (2θ) of 0 and 24.3°, respectively. The boundaries of the experimentally determined maximum and minimum energy are indicated by the dot–dash lines.

parts of the temperature-dependent scattering pattern. The spatial distribution of the observed inelastic scattering is consistent with the shape of the (100) section of the Brillouin zone of silicon. The same conclusion can be made for the measurements of Beddoe *et al.* (1983) for a [111] direction. Wu *et al.* (1999) have also observed similar effects in a non-energy analysed diffuse X-ray scattering study of silicon for a [111] direction.

A general conclusion is that the separation of elastic and inelastic scattering of neutrons is important if the elastic scattering is weak (*e.g.* if the elastic scattering arises from low concentrations of small precipitates). As far as the authors know, nearly all SANS experiments involve the measurement of the total differential scattering cross section (*i.e.* elastic + inelastic). Fig. 13 shows the radially averaged cross sections obtained from a silicon crystal containing low concentrations of small SiO_2 precipitates. It is clear from this figure that the contribution of the inelastic scattering to the total scattering is significant and could lead to erroneous results. The inelastic contribution can be subtracted if the total scattering from a control sample with no SiO_2 precipitates is also measured (see Fig. 14). If the samples are single crystals, this subtraction requires that the control sample and precipitate-containing samples must be accurately positioned so that the neutron beam impinges along the same crystallographic axis in both crystals. Small differences in sample and control alignment are probably the origin of the significant scatter in the cross-section points apparent when the control sample is subtracted
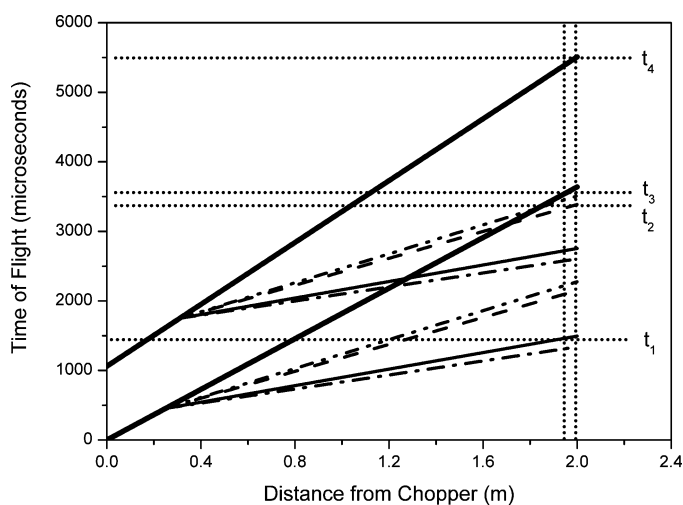
from the precipitate-containing silicon sample (Fig. 14). It is also crucial that the presence of the SiO_2 precipitates does not alter either the shape or the magnitude of the inelastic scattering. This later point also applies if measurements are made on polycrystals where the alignment would not be so important.
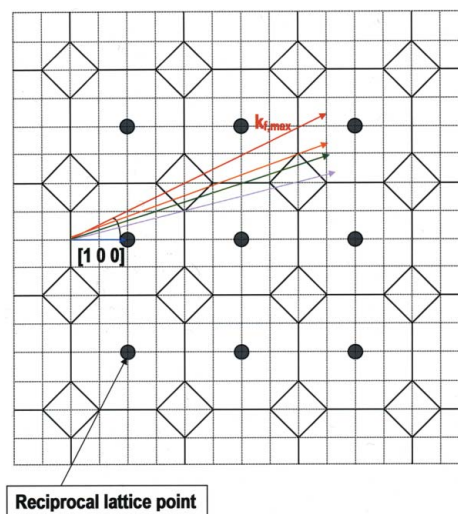

Figure 12
The upper diagram is a two-dimensional representation of the extended Brillouin zone of a face-centred cubic lattice (100) section. The magnitude of the scattered wavevector $k_{f,max}$ corresponds to the maximum value of k_f arising from the annihilation of a phonon with the maximum possible energy in silicon of ~66 meV ($\omega \simeq 100$ Trad s^{-1}). The lower diagram is the measured anisotropic inelastic scattering.

Figure 11
Time-of-flight graph of the neutron paths for neutrons detected at the edge of the detector that have gained energy from phonons. The lower thick line is for the fastest elastically scattered neutron at the start of the chopper pulse and the upper thick line is for the slowest elastically scattered neutron at the end of the chopper pulse. The sample is between 0.25 and 0.31 m from the chopper; the graphs for the fastest and slowest incident neutrons gaining 13.2 meV are shown by the thin lines, and the graphs for the fastest and slowest incident neutrons gaining 4.5 meV are shown by the dashed lines. The dot–dash lines and the dot–dot–dash lines are, respectively, for neutrons gaining more than 13.2 meV or less than 4.2 meV. The vertical dotted lines show the spatial region over which the detector can detect neutrons ($t_1 = 1494$ μs, $t_2 = 3310$ μs, $t_3 = 3639$ μs, $t_4 = 5508$ μs).
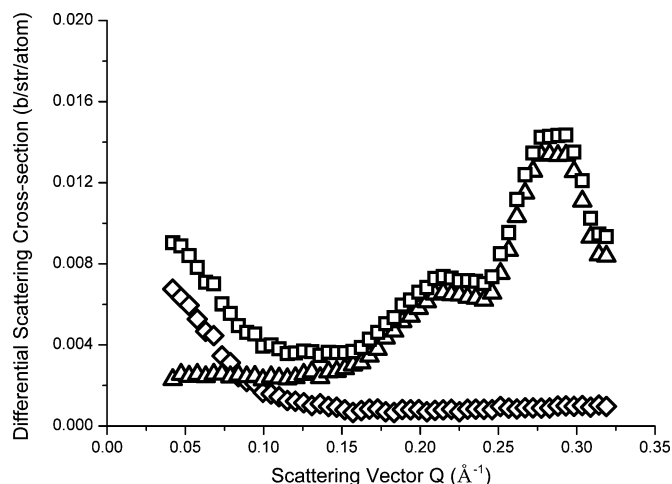

Figure 13
The radially averaged differential scattering cross sections from a silicon single crystal containing a low concentration of SiO_2 precipitates. The square symbols represent the total scattering (elastic + inelastic), the triangular symbols the inelastic scattering and the diamond symbols the elastic scattering.
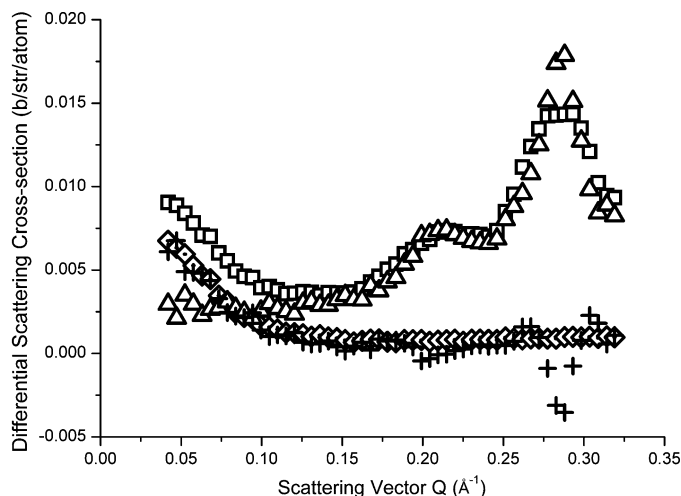
Figure 14
The radially averaged differential scattering cross sections from a silicon single crystal containing a low concentration of SiO_2 precipitates (*A*) compared with that of a control silicon sample containing no SiO_2 precipitates (*B*). The square symbols represent the total scattering (elastic + inelastic) from sample *A* and the triangular symbols the total scattering from sample *B*. The diamond symbols represent the elastic scattering from sample *A* and the crosses the total scattering from sample *A* minus the total scattering from sample *B*.

6. Conclusions

These measurements have established that the temperature-dependent neutron scattering observed in silicon single crystals for small scattering vectors is an inelastic process. To satisfy energy and momentum conservation in the interaction between the incident neutrons and the crystal phonons, an Umklapp process is needed in which the neutron gains energy in the range 4.5–13.2 meV from a phonon.

References

Beddoe, R. E., Messoloras, S., Stewart, R. J., Kostorz, G. & Mitchell, E. W. J. (1983). *Philos. Mag.* **48**, 935–952.
Dolling, G. (1963). *Neutron Inelastic Scattering*, Vol 2, pp. 37–48. Vienna: International Atomic Energy Agency.
Gupta, S., Messoloras, S., Stewart, R. J. & Schneider, J. R. (1992). *J. Phys. Condens. Matter*, **4**, 5383–5390.
Ibel, K. (1976). *J. Appl. Cryst.* **9**, 296–309.
May, R. P. (2000). http://www.ill.fr/YellowBook/D22.
Wu, Z., Hong, H., Aburano, R., Zschack, P., Jemian, P., Tischler, J., Chen, H., Luh, D. A. & Chiang, T. C. (1999). *Phys. Rev. B*, **59**, 3283–3286.